The Linkage between the Warm and the Cold Conveyor Belts in an Idealized Extratropical Cyclone

Author(s):
Schemm, Sebastian; Wernli, Heini

Publication date:
2014-04

Permanent link:
https://doi.org/10.3929/ethz-b-000082829

Originally published in:
Journal of the Atmospheric Sciences 71(4), https://doi.org/10.1175/JAS-D-13-0177.1

The Linkage between the Warm and the Cold Conveyor Belts in an Idealized Extratropical Cyclone*

SEBASTIAN SCHEMM AND HEINI WERNLI

Institute for Atmospheric and Climate Science, ETH Zürich, Zurich, Switzerland

(Manuscript received 14 June 2013, in final form 24 November 2013)

ABSTRACT

This study continues the investigation of airstreams in idealized moist baroclinic waves and addresses the formation of the cold conveyor belt (CCB), its linkage to the warm conveyor belt (WCB), and their impact on the development of a midlatitude cyclone. The CCB is identified as a coherent bundle of trajectories, characterized by weak ascent and a strong increase of potential vorticity (PV) along the flow, in contrast to the WCB, defined as the trajectories with maximum ascent. The authors illuminate the role of the two conveyor belts in the formation of two strong PV anomalies that form in the upper (WCB, negative PV anomaly) and lower troposphere (CCB, positive PV anomaly), respectively, and thereby establish a link between these airstreams and relevant aspects of the dynamics of extratropical cyclones. The CCB moves close to the surface along the colder side of the bent-back front and experiences a PV increase as it passes below a region of maximum latent heat release at midtropospheric levels. Accordingly, it arrives with high PV values at the tail of the bent-back front where the most intense low-level winds occur. The WCB, which rises above the bent-back front, causes the formation of the midtropospheric heating rate maximum and thereby not only influences the upper-level downstream development, but also drives the increase of PV along the CCB and, in consequence, indirectly drives the formation of the low-level jet at the tail of the bent-back front.

1. Introduction

a. The Lagrangian perspective on extratropical cyclones

Studies of coherent ''air currents'' have a long tradition in the field of dynamic meteorology, dating back at least to the model of warm and cold air currents by Bigelow (1902). Bigelow described alternating streams of rising warm and moist tropical air masses east of a surface depression and sinking polar air masses west of the depression as coherent currents. One convenient possibility to study and visualize the motion of such coherent air masses that ascend or descend within a propagating system is the calculation of trajectories. The calculation of trajectories was already applied by Shaw and Lempfert (1906) to observations close to the surface, and it has become a widely used diagnostic of midlatitude flow systems ever since. Several studies in the beginning of the twentieth-century applied ''trajectory like'' diagnostics assuming, for example, the conservation of potential temperature θ or absolute vorticity (Namias 1939). Later, the depiction of streamlines on surfaces of constant potential temperature was utilized (Green et al. 1966), which revealed the dry adiabatic motion in a developing cyclone. The analysis of isentropic trajectories, which correspond to the actual flow if it is bounded on an isentropic surface, identified three principal airstreams (Carlson 1980). These airstreams, defined as coherent bundles of trajectories, share similarities in the temporal evolution of various parameters such as θ or pressure. They are the warm conveyor belt (WCB) and the cold conveyor belt (CCB), which we describe in the next paragraph in more detail, and the dry air intrusion, which is descending behind the cold front from upper-tropospheric or lower-stratospheric altitudes and, precisely speaking, is not denoted as a conveyor belt. From the Lagrangian perspective, the conveyor belts are understood as coherent bundles of air

Denotes Open Access content.

* Supplemental information related to this paper is available at the Journals Online website: http://dx.doi.org/10.1175/JAS-D-13-0177.s1.

Corresponding author address: Sebastian Schemm, Institute for Atmospheric and Climate Science, Universitästrasse 16, 8092 Zurich, Switzerland.
E-mail: sebastian.schemm@env.ethz.ch

DOI: 10.1175/JAS-D-13-0177.1

trajectories, which share similarities in their evolution along the flow (Wernli and Davies 1997). Early case studies of extratropical cyclones with a strong focus on trajectories and their temporal evolution have been performed, for example, by Whitaker et al. (1988), Kuo et al. (1992), Stoelinga (1996) and Wernli (1997), based on reanalysis or numerical simulation data. More recently, Eckhardt et al. (2004) and Madonna et al. (2014) made use of trajectories to perform climatologies of WCBs. Other studies used trajectories to investigate microphysical processes along the warm conveyor belt (Joos and Wernli 2012) and other small-scale transient structures within extratropical cyclones such as sting jets (Clark et al. 2005; Martínez-Alvarado et al. 2010).

b. *The conveyor belt model*

The conveyor belt model describes the life cycle of a midlatitude cyclone by the evolution of three principal airstreams: the WCB, the CCB and the dry intrusion. The focus of this conceptual model lies on the three-dimensional structural evolution of the developing depression. The conveyor belt terminology was introduced in the studies of Harrold (1973), Carlson (1980), and Young et al. (1987) and was fostered in a series of publications by Browning (Browning 1986, 1990; Browning and Roberts 1994). Here we give a brief description of the model following Browning (1990).

The WCB is a coherent bundle of moist warm air moving poleward in the warm sector along the cold front, which is vigorously rising along frontal zones. We commonly distinguish two types of WCBs. WCBs of type 1 rise along the cold front (WF1), while WCBs of type 2 rise above the bent-back extension of the surface warm front, which we refer to as the bent-back front (WF2; Browning and Roberts 1994; Bader et al. 1995; Browning 2004; Agustí-Panareda et al. 2009). At upper levels, the WCB fans out, parts of it turn cyclonically and others anticyclonically, and it typically forms the cloud head of the cyclone. The region where the WCB fans out is referred to as the outflow. The cyclonic path of the WCB, which ascends above the warm front, is studied also as a ''trowal'' airstream because of its thermal structure at upper levels which forms a ''trough of warm air aloft'' (Crocker et al. 1947; Godson 1951; Penner 1955; Galloway 1958; Martin 1999).

On a satellite image, the WCB is typically visible as an elongated cloud band (Browning 1986) above a frontal region. WCBs contribute to the ventilation of the boundary layer and the transport of boundary layer moisture into the free troposphere (Stohl 2001; Sinclair et al. 2008). They have been described to be responsible for some of the characteristic features in zonal mean moisture profiles (Boutle et al. 2011). In midlatitudes, they form the majority of large-scale precipitation (Browning 1986; Wernli 1997). A 15-yr WCB climatology of Eckhardt et al. (2004) showed that WCBs are frequent features of extratropical cyclones, for example, 60% of all winter cyclones in the Northern Hemisphere are associated with a WCB.

For an eastward-moving cyclone, the CCB typically moves against the direction of propagation at low levels, along the warm front and its bent-back extension. The CCB is situated at the colder side of the front that separates the CCB from the ascending WCB. One branch of the CCB slopes cyclonically at low levels into the center of the depression, while a second branch turns anticyclonically and ascends into the cloud head (Carlson 1980; Browning 1990). The cyclonic branch typically is associated with strong low-level winds along the bent-back front, often in the form of a low-level jet. The anticyclonic branch of the CCB is described in the literature to rise from lower levels into the cloud head after turning anticyclonically at some point during its motion along the bent-back front (Carlson 1980; Whitaker et al. 1988). The review by Schultz (2001) gives a concise overview on ambiguities and the complexity associated with an accurate definition of the CCB. Schultz (2001) concluded that the anticyclonic path of the CCB should more appropriately be described as a ''transition'' airstream between the WCB and the cyclonic branch of the CCB.

c. *The process of selecting WCB and CCB trajectories*

To select WCB trajectories, a suitable selection criterion is the one of strong ascent (e.g., 600 hPa within 48 h), with a starting position in the vicinity of an extratropical cyclone (Wernli and Davies 1997). Wernli and Davies (1997) also showed that, besides a maximum decrease of pressure, the maximum decrease of specific humidity or maximum increase of potential temperature results in the selection of similar WCB trajectories. In contrast, a Lagrangian criterion to select the CCB from a large ensemble of trajectories has not been proposed yet. To select trajectories that are representative for the CCB, we have to translate more ''figurative'' descriptions of the CCB in the previous literature, for example, ''the air ahead of and beneath the warm front which, relative to the advancing system, flows rapidly rearwards around the poleward side of the low centre'' (Browning and Roberts 1994, p. 1536), into a Lagrangian selection criterion.

Previous studies of the CCB showed or analyzed a selection of a few trajectories, which were considered to be representative for the flow based on their shape or origin (Kuo et al. 1992; Schultz and Mass 1993; Mass and Schultz 1993; Reed et al. 1994; Schultz 2001). In this study, we attempt to establish a formal Lagrangian

selection criterion for the CCB. For example, Schultz (2001) described the origin of the CCB to be in the lower troposphere. Later, the CCB passes underneath the warm-frontal zone. Its cyclonic branch remains, according to Schultz (2001), at lower levels and turns cyclonically around the center of the low. Accordingly, we require the CCB trajectories to remain close to the surface. Additionally, Schultz (2001, p. 2208) suggested that "potential vorticity is created in the cold conveyor belt beneath the area of latent heat release in the ascending warm conveyor belt." Therefore, we require potential vorticity (PV) to increase along a CCB trajectory above a certain threshold. The height below which the CCB starts and ends and the threshold above which PV needs to increase once along a CCB trajectory are the two degrees of freedom of our Lagrangian selection criterion. In section 4a, we give a short outline and justification for our choices. For the time period of interest, we suggest to analyze the same 48 h as for the WCB. We recognize that, given the above criteria, we select only a subcategory of air parcels that are flowing cyclonically below the warm front, which is a common descriptive CCB criterion (Carlson 1980; Browning and Roberts 1994; Schultz 2001). However, from a PV perspective of diabatic impacts on the intensity and structure of cyclones, the above criteria select the trajectories that have a particularly large impact, as further discussed in section 4a. Also, we note that, by definition, our Lagrangian CCB selection criterion is not capable of identifying any ascending anticyclonic path of the CCB.

d. PV framework and diabatic PV modification

The PV perspective provides a powerful framework in the analysis of midlatitude cyclones and their dynamics (Hoskins et al. 1985). Past studies characterized the evolution of extratropical cyclones in terms of three distinct positive PV anomalies (Davis and Emanuel 1991): a surface potential temperature anomaly, which acts as a surrogate for potential vorticity, a midtropospheric PV anomaly, and an upper-level PV anomaly of stratospheric air. All three anomalies are influenced by characteristic diabatic processes, which are surface fluxes at lower levels, latent heating in clouds, and radiation at mid- and upper-tropospheric levels. These anomalies can act as a catalyst for strong storm intensification, especially in case of their vertical alignment into a "PV tower." Such PV towers have been frequently reported in case studies of severe storms (Reed et al. 1992; Rossa et al. 2000; Wernli et al. 2002) and studied climatologically by Čampa and Wernli (2012). In particular, the release of latent heat by condensation is one of the key mechanisms behind the intensification of midlatitude cyclones and the PV framework has been used successfully to describe this process (Davis and Emanuel 1991; Kuo et al. 1992; Stoelinga 1996; Wernli 1997). It is also adopted in this study.

The material change of PV due to diabatic heating is described by the PV tendency equation (Hoskins et al. 1985; Haynes and McIntyre 1987):

$$\frac{D}{Dt}\mathrm{PV} = \frac{1}{\rho}[(2\Omega + \nabla\times\mathbf{V})\cdot\nabla\dot{\theta} + \nabla\theta\cdot(\nabla\times\mathbf{F})]. \quad (1)$$

The vector $\mathbf{F}$ collects all nonconservative forces, for example, turbulent friction and numerical diffusion effects. The vector $\mathbf{V}$ denotes the three-dimensional wind vector, $D\theta/Dt = \dot{\theta}$ is the diabatic heating rate, and ρ is the density. For large-scale ascent, the vertical component of the scalar product becomes the dominant term, and we recast Eq. (1) by neglecting frictional forces, as

$$\frac{D}{Dt}\mathrm{PV} \approx \frac{1}{\rho}\eta\left(\frac{\partial\dot{\theta}}{\partial z}\right), \quad (2)$$

where $\eta = \zeta + f$ denotes the vertical component of the absolute vorticity and $f = 2\Omega\sin(\phi)$ is the Coriolis parameter. Hence, from Eq. (2) it follows that an air parcel below the level of maximum heating, where $\partial\dot{\theta}/\partial z > 0$, will increase its PV value and decrease it above (Eliassen and Kleinschmidt 1957; Haynes and McIntyre 1987; Raymond and Jiang 1990; Wernli and Davies 1997; Brennan et al. 2008). The formation of a negative PV anomaly at upper levels related to WCB outflows has been reported to be significant for perturbations of the Rossby waveguide (Pomroy and Thorpe 2000) and quantified climatologically by Madonna et al. (2014). As previously shown, in a case study over the North Atlantic (Grams et al. 2011) and in an idealized simulation (Schemm et al. 2013), the development of a secondary cyclone downstream can be enhanced by waveguide perturbations induced by low-PV air masses in the WCB outflow.

The diabatic modification of PV thus can give illuminating insight into the growth of a midlatitude system. In this study, we investigate the temporal evolution of PV along trajectories that we then associate with WCB and CCB flows.

e. Scope and structure of this study

It is the main objective of this study to assess, from a Lagrangian perspective, the impacts of diabatically produced PV anomalies, in coherent WCB and CCB flows, on the dynamics of an idealized extratropical cyclone. We perform a set of two different idealized simulations. In the highly idealized simulation, in the following referred to as the idealized run, we restrict the

physical processes to condensation and evaporation, which henceforth act as the only diabatic source term of PV (besides the influence of numerics). The absence of a subgrid-scale parameterization of turbulence, moist convection, radiation, and surface fluxes bounds the simulation closely to the pure dry dynamical evolution of the flow. The second simulation incorporates parameterizations of microphysical processes such as the formation and evaporation of rain, turbulence, convection, and surface heat and momentum fluxes. This extended-physics simulation, referred to as the extended run, uses the exact same initial conditions as the idealized run and mainly acts as a robustness test for our findings.

Our main research objectives for this study are

- to specify a Lagrangian selection criterion for identifying CCB trajectories (as previously done for the WCB, with the criterion of maximum ascent);
- to describe and explain the temporal evolution of a number of parameters, in particular PV, along both conveyor belts, with a focus on the CCB;
- to study the interaction of the WCB and the CCB and show the inherent linkage between the two; and
- to summarize these findings in a conceptual schematic of a WCB, a CCB, and their associated PV anomalies.

After introducing the simulations and their initial conditions in section 2, we give a synoptic overview of the simulation in section 3. A pressure–PV scatterplot and the selection criteria for the WCB and CCB are presented in section 4, where also the temporal evolution of PV and other parameters along the WCB and CCB is studied in greater detail. In section 5, we show how the temporal PV changes along the WCB and CCB are inherently linked to each other. We conclude with a summary in section 6.

2. Model setup

Both simulations use the same initial conditions on an f plane ($\sim 1.03 \times 10^{-4}\,\mathrm{s}^{-1}$) with periodic boundary conditions in the zonal direction. We use a channel version of the Consortium for Small-Scale Modeling (COSMO) model with a zonal extent of 16 800 km and a meridional extension of 8400 km. The horizontal grid spacing is 0.18° (~21 km), and in the vertical the model extends to 12 km using 60 vertical levels. Below, we give a brief overview of the initialization; for a more detailed description, the reader is referred to Schemm et al. (2013).

a. Idealized simulation

The atmosphere is initially prescribed with a zonally uniform jet stream in thermal wind balance. The three-dimensional pressure distribution is obtained from the hydrostatic balance equation, starting with a meridional temperature profile at a reference altitude. At the surface, the temperature in the center of the domain is around 281 K, with a total north–south variation of approximately 17 K. The tropospheric lapse rate at the center of the domain is $5.2\,\mathrm{K\,km}^{-1}$, and the stratospheric lapse rate is $0.3\,\mathrm{K\,km}^{-1}$. The obtained maximum wind speed is about $40\,\mathrm{m\,s}^{-1}$, and the mean tropopause height is 8.5 km.

The initial moisture is defined using a relative humidity (RH) profile starting with 60% at the bottom and a linear vertical decrease of $5\%\,\mathrm{km}^{-1}$. Vertical cross sections of the initial conditions are shown in Fig. 1 of Schemm et al. (2013). In the idealized simulation, a free-slip lower boundary condition is used, and condensation of water vapor or evaporation of cloud water is taken into account by saturation adjustment, which can produce warm, nonprecipitating clouds.

To perturb the zonally uniform basic state, we place a PV anomaly with an amplitude of 2 PVU ($1\,\mathrm{PVU} = 10^{-6}\,\mathrm{m^2\,s^{-1}\,K\,kg^{-1}}$) in the vicinity of the jet and run a quasigeostrophic PV inversion to obtain perturbation fields for wind, temperature, and pressure.

During the first days of the simulation, a primary cyclone [see Fig. 2 of Schemm et al. (2013)] grows. By day 5, the growth of a second cyclone downstream of the initial cyclone starts because of wave dispersion. This downstream cyclone follows fairly closely the conceptual evolution described by Shapiro and Keyser (1990), and we use this downstream cyclone for the identification of the conveyor belts in this study. Its synoptic evolution is described in more detail in section 3.

b. Extended simulation

The set of schemes used for the extended physics simulation is in operational use in the global model of the German Weather Services (DWD) and is tested thoroughly for grid spacings of 20–30 km. The only difference to the operational setup is that ice-phase processes are excluded from the microphysics scheme. By doing so, we add only one more water category, that is, rain, and thereby simplify the comparison with the results from the idealized run. We recognize that ice-phase processes can also lead to changes in the PV field (Joos and Wernli 2012), but for the reason of simplicity, they are not included in this study. A brief overview of the used parameterizations is given below. For more details, the reader may refer to the COSMO core documentation: www.cosmo-model.org/content/model/documentation/core/default.htm. The schemes used are as follows.

- The Kessler microphysics warm-rain parameterization without ice-phase processes (Kessler 1969). First,

water vapor is transferred into cloud water, in the case of saturation, before autoconversion and aggregation lead to the formation of rain droplets. They can leave the cloud if their sedimentation velocity becomes larger than grid-scale vertical velocity. In the case of unsaturated air below the cloud, rain droplets can evaporate, which in turn leads to below-cloud diabatic cooling.

- A turbulent kinetic energy (TKE)–based turbulence parameterization (Herzog et al. 2002) that calculates turbulence coefficients for heat and momentum and includes subgrid-scale condensation and evaporation. The surface flux parameterization follows Mellor and Yamada (1982).
- The Tiedtke mass flux scheme for moist convection (Tiedtke 1989). Evaporation of cloud droplets in strong downdraft regions is also accounted for in the scheme by the saturation adjustment.

The temperature tendency due to conversion between the three water categories is

$$\frac{\partial T}{\partial t} = \frac{L_v}{c_p}(S_c - S_e), \tag{3}$$

where L_v denotes the latent heat of vaporization and c_p denotes the specific gas constant. The variable S_c is condensation of vapor q_v to cloud water q_c, and S_e is the evaporation of q_c and rain q_r to q_v. Therefore, diabatic PV changes are expected not only in regions where cloud droplets form, but also in regions where rain droplets evaporate. For example, rain droplets formed during the ascent of the WCB may fall into a region of subsaturated air below the WCB, where the CCB is located (see below).

The extended simulation is performed over an ocean surface, and the sea surface temperature is set to the initial temperature at the lowest model level and kept constant during the simulation. No radiation scheme is used.

3. Simulation overview

For both simulations, we focus on the temporal evolution of the downstream cyclone, shown in Fig. 1. In Figs. 1a and 1b, sea level pressure (dashed contours), potential temperature (solid contours), specific humidity q_v (coloring) at 850-hPa level, and the dynamical tropopause (2 PVU) on 320 K (red contour) are depicted for the idealized simulation and in Figs. 1c and 1d for the extended simulation.

In Fig. 1a, the idealized cyclone has grown an elongated bent-back front and an intense eastward-moving cold front. In the warm sector along the cold front, q_v reaches 9 g kg^{-1} and a tongue of moist, warm air extends from the warm sector along the bent-back front around the center of the depression. At upper levels, a trough of stratospheric air elongates southward behind the surface cold front. Downstream, a tropospheric ridge extends poleward and starts to bend cyclonically.

Cyclonic wave breaking of the trough becomes evident 10 h later (Fig. 1b). The system reaches its mature stage, during which the bent-back front wraps up behind the cold front. During this stage, along the bent-back front, warm, moist air decouples from the warm sector and forms a warm-air seclusion. Along the cold front, q_v increases further because of isentropic advection of warm and moist air masses. Given the strong horizontal pressure gradient along the bent-back front, strongest surface winds are expected in this region.

For the extended run, we consider a time period during which the cold front and the CCB occur with comparable strength to that in the idealized run. However, during this period the upper-level evolution shows a much more advanced cyclonic wave breaking in the extended case (Fig. 1c), and the WCB is stronger (see below). In the warm sector along the cold front, slightly higher values of q_v (10 g kg^{-1}) are found. The bent-back front appears much weaker than in the idealized run, and additionally, it is decoupled from the warm sector. Therefore, the air along the bent-back front and its tail is much drier, and no warm-air seclusion forms at 850 hPa. Instead, at higher altitudes between 850 and 700 hPa, the warm front is stronger and a weak seclusion of warm air occurs, as can be seen in a vertical cross section through the bent-back front discussed later (Fig. 7b). Surface friction and cooling due to downward sensible heat fluxes are inhibiting the formation of a warm-air seclusion in the extended simulation, a result that is in accordance with earlier findings of Hines and Mechoso (1993), Thompson (1995), and Rotunno et al. (1998). One day later (Fig. 1d), the bent-back front is stronger but remains less pronounced than in the idealized run, especially along its northern part. As a consequence of the reduced pressure gradient there, the wind speed along the tail of the front is weaker. Behind the cold front, small disturbances in the moisture field suggest the occurrence of shallow convection.

4. Diabatic PV changes from a Lagrangian perspective

a. A Lagrangian pressure–PV scatterplot

The analysis of trajectories provides a useful framework to assess diabatic PV changes within a growing

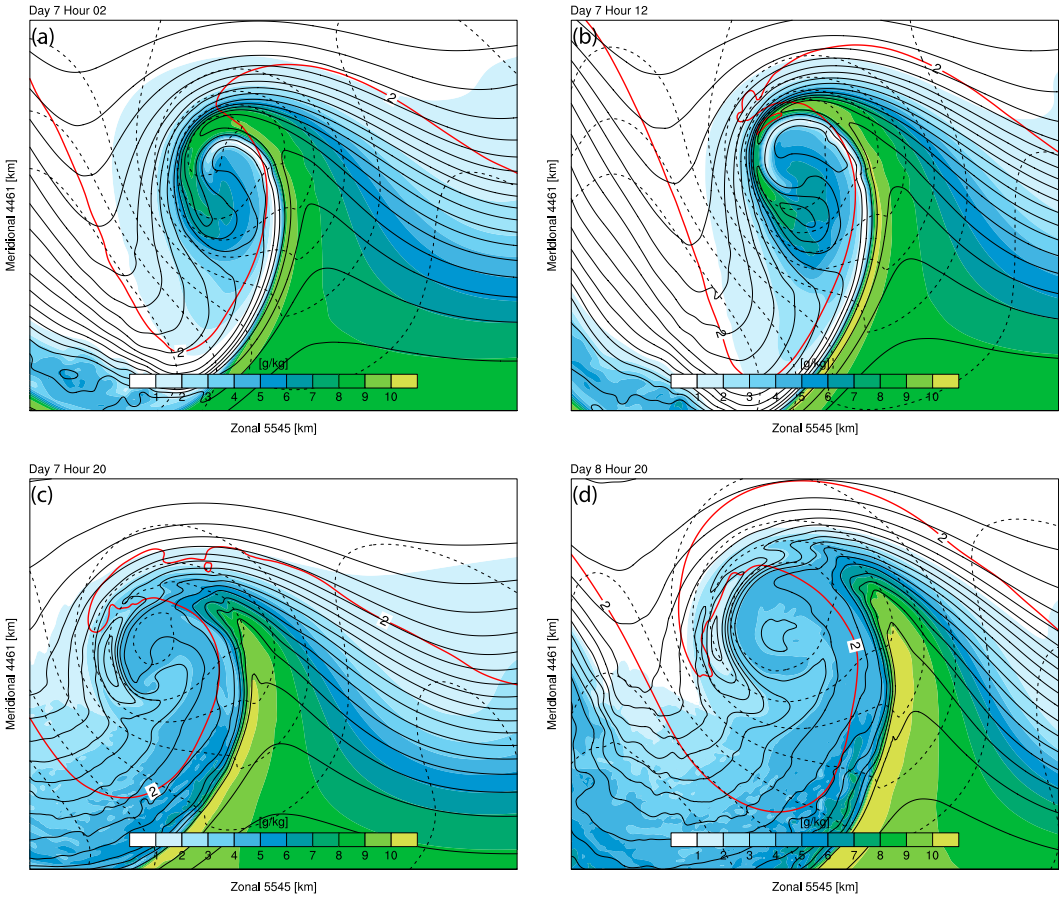

FIG. 1. Synoptic overview of the (a),(b) idealized and (c),(d) extended simulations. Shown are surface pressure (dashed contours; hPa), potential temperature (solid; K), and specific humidity (colors; g kg^{-1}) at 850 hPa. Red solid contours show the dynamical tropopause (2 PVU) on 320 K.

depression. As a starting point for our analysis, we construct a scatterplot of diabatic PV and pressure changes along a large ensemble of trajectories. For this pressure–PV scatterplot, forward trajectories are calculated for both simulations over a time period of 2 days starting at every grid point below 800 hPa, where most of the moisture is contained in the simulation. We focus on two 48-h periods (as discussed above) for the idealized simulation from day 6 to day 8 and for the extended simulation from day 7 to day 9, where we identify a comparable number of CCB trajectories as shown below. The influence of the choice of the time period on the results is discussed later.

The pressure–PV scatterplot shows on the y axis the total pressure change along the trajectories, that is, the pressure at the starting position of the trajectory minus the pressure at the final position. The x axis shows the PV anomaly at the final trajectory position. The anomaly is defined as the difference to the unperturbed initial conditions. We show the result for the idealized simulation in Fig. 2a and for the extended simulation in Fig. 2b. Both diagrams show a clear tendency to form negative PV anomalies for air parcels that ascend more than about 450 hPa.

For the idealized simulation (Fig. 2a), the majority of air parcels show pressure changes of 100 hPa or less and comparatively small PV anomalies (with absolute values of less than 0.75 PVU). Most of the trajectories with a strongly positive PV anomaly have a weak ascent of 200 hPa or less. This can be understood from the approximated PV tendency equation given in Eq. (2). In case of a weak ascent, the air parcels remain continuously below the region of maximum diabatic heating found at midtropospheric levels, and their PV increases without ever reaching regions of negative vertical heating rate gradients. In contrast, air parcels that ascend more than 250 hPa reach levels with a negative diabatic PV tendency above the midtropospheric heating rate maximum and typically form a negative anomaly with respect to the initial conditions. Air parcels that ascend even

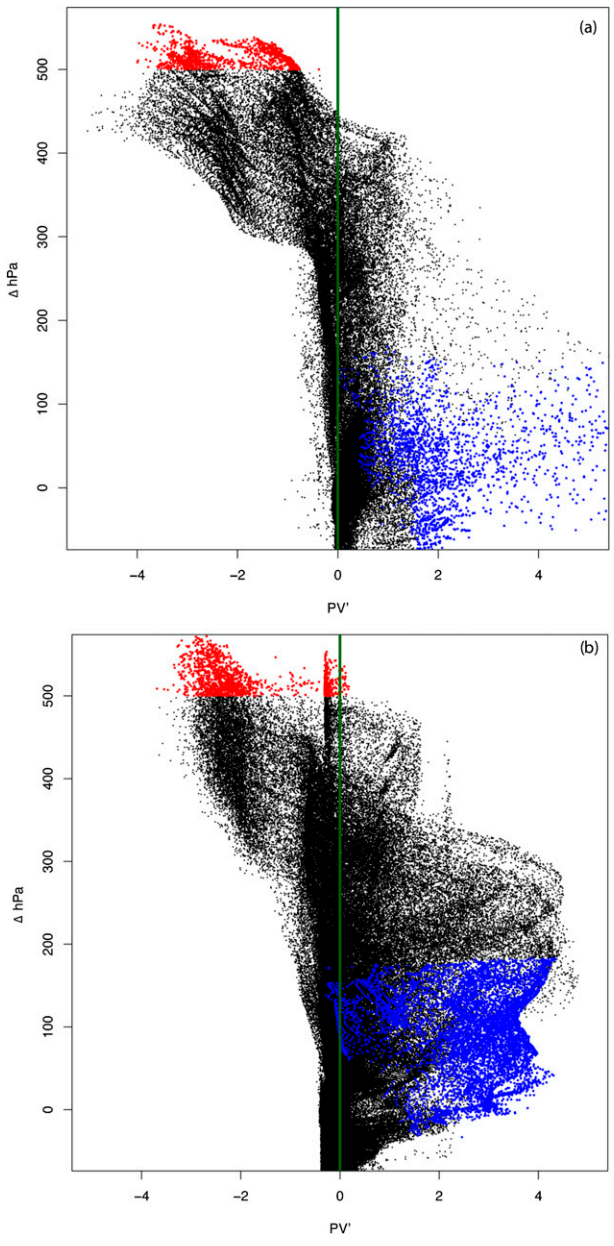

FIG. 2. Lagrangian pressure–PV scatterplot for the (a) idealized and (b) extended runs. Along the y axis, the total pressure change ΔP (hPa) over a period of 48 h along every trajectory starting from below 800 hPa in the warm sector of the cyclone (y-axis range from −50 to 550 hPa) is shown; along the x axis, the PV anomaly PV′ (PVU) at the final trajectory position, defined as the difference to the unperturbed initial conditions, is shown. Air parcels with strongest ascent (WCB) are colored in red, and air parcels that are selected according to the CCB criteria are colored in blue.

more than 400 hPa show an enhanced negative PV anomaly. These air parcels are, at the end of the 48-h period, located above the initial altitude of the troposphere, which leads to negative PV anomalies exceeding −2 PVU. Therefore, we find very strong negative PV anomalies for the strongest ascending trajectories.

In summary, Fig. 2a indicates that for air parcels rising from below 800 hPa, the formation of strong positive PV anomalies is limited to air parcels that remain at low levels and the formation of strong negative PV anomalies is limited to those that ascend to upper levels.

For the extended simulation (Fig. 2b), the pressure–PV scatterplot is qualitatively similar but shows much more variability. In particular, the number of air parcels that undergo strong positive PV changes is significantly higher compared to the idealized run (Fig. 2a). In the extended simulation also, air parcels that ascend by approximately 300 hPa (or less) are associated with strong positive PV anomalies. Again, this is related to their position relative to the region of maximum latent heating, which in this simulation extends to higher levels, and is less coherent, with two distinct maxima at low and midtropospheric levels (see Fig. 7b). The strongest negative PV anomalies occur, as previously, for strongly ascending trajectories. The air parcels with strong ascent form a coherent patch in the scatterplot with strongly negative PV anomalies, except for a minor branch that shows almost no PV anomaly. This smaller branch crosses the dynamical tropopause and experiences a diabatic increase of PV to stratospheric values, and, consequently, does not show a strong negative PV anomaly with respect to the initial conditions. As radiation is turned off in our simulation and TKE is found to be strong along these air parcels (not shown), the increase in PV is most likely associated with turbulent mixing with stratospheric air in a region with a large vertical wind shear (Shapiro 1976, 1978; Keyser and Rotunno 1990).

This pressure–PV scatterplot now allows us to identify important subcategories of trajectories with a near-surface origin, which are relevant for the formation of very strong negative and positive PV anomalies. The first category is the WCB, which we select with the previously introduced Lagrangian criterion of maximum ascent (section 1c), here with a threshold of 500 hPa within 2 days. Thus, we select the air parcels colored in red (Fig. 2a), which are associated with a strongly negative PV anomaly at upper levels. In the idealized simulation, the number of trajectories that ascend 500 hPa or more is around 1300 and for the extended simulation is around 1500.

The second category contains the trajectories that meet the previously given Lagrangian selection criterion for the CCB (section 1c). They are required to start and end at low levels and increase their PV above a certain PV threshold during the 2-day period at least once. After the PV threshold is exceeded along the flow, PV is

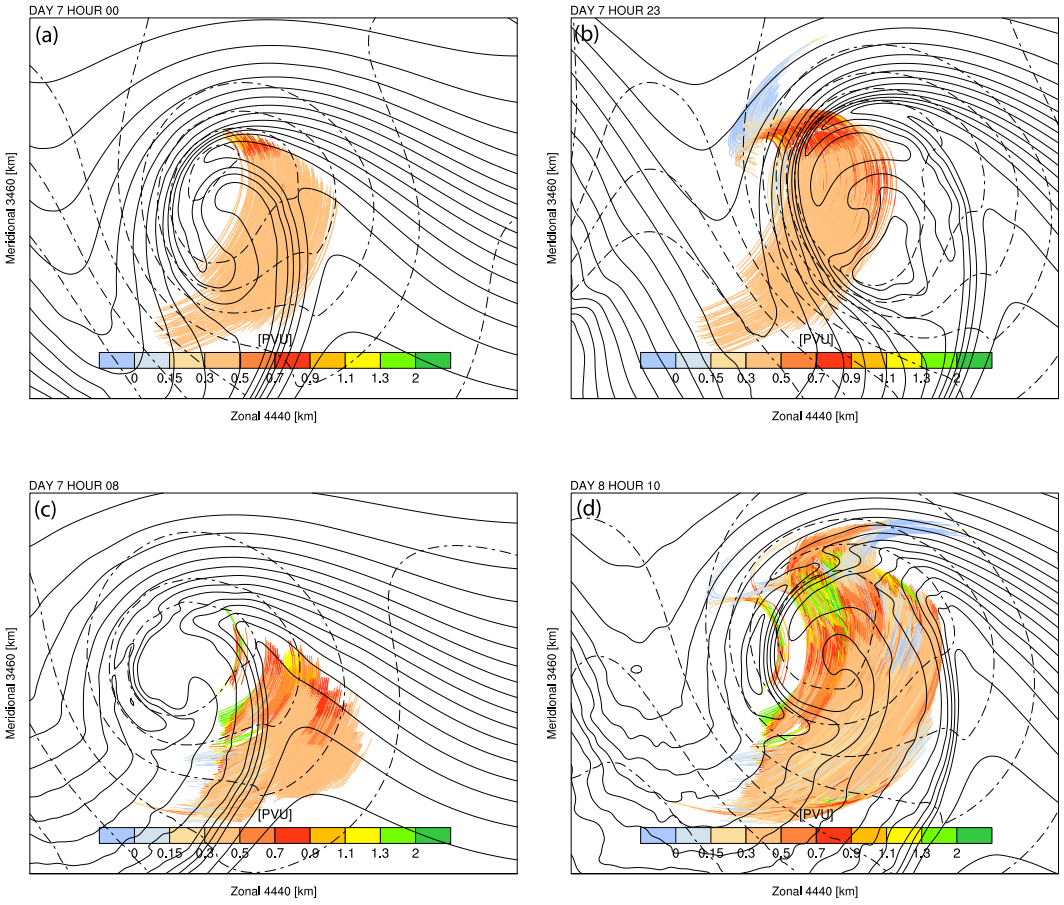

FIG. 3. WCB trajectories colored with PV for the (a),(b) idealized and (c),(d) extended simulations. Solid lines show contours of potential temperature at 850 hPa in steps of 2 K, and dashed contours show surface pressure (hPa) in steps of 10 hPa. Around 1300 trajectories are found for the idealized case and around 1500 trajectories are found for the extended case.

allowed to increase further, stay constant, or even decrease again to values below the threshold. We defined the start and end values of pressure to be below 800 hPa and the PV threshold to be 2 PVU. The selected air parcels are colored in blue in Fig. 2. They are associated with strongly positive PV anomalies at the end of the 2-day period (which was not explicitly required by the selection criterion) and only moderate changes of pressure between their start and end times. The number of CCB trajectories is in both simulations around 1500.

Therefore, according to Fig. 2, we selected with the two Lagrangian criteria for WCBs and CCBs, two specific flow features that are important to characterize the impact of diabatic processes on the life cycle of the cyclone from the PV perspective. In the following subsections, we have a closer look at the paths and the temporal evolutions of pressure, PV, and other parameters along the selected WCB and CCB trajectories.

b. Principal airstream 1: The WCB

The selected WCB trajectories are shown in Fig. 3a for the idealized simulation, with colors indicating the trajectories' PV values. The corresponding Lagrangian evolution of pressure, potential temperature, specific humidity, and PV was studied already in detail in Schemm et al. (2013). Initially, the poleward motion is adiabatic, with PV values of about 0.36 PVU. The WCB is moving northward at low levels into the frontal fracture region, and, when reaching the bent-back front at day 7, hour 0 (Fig. 3a), vertical motion along steep isentropes leads to saturation and to the release of latent heat due to condensation. The location of the WCB below the maximum of latent heat release at midtropospheric levels results in an increase of PV up to 0.9 PVU (red coloring in Fig. 3a) at day 7, hour 2.

When the WCB reaches upper levels (Fig. 3b), a typical diffluence of the flow into the cloud head of the

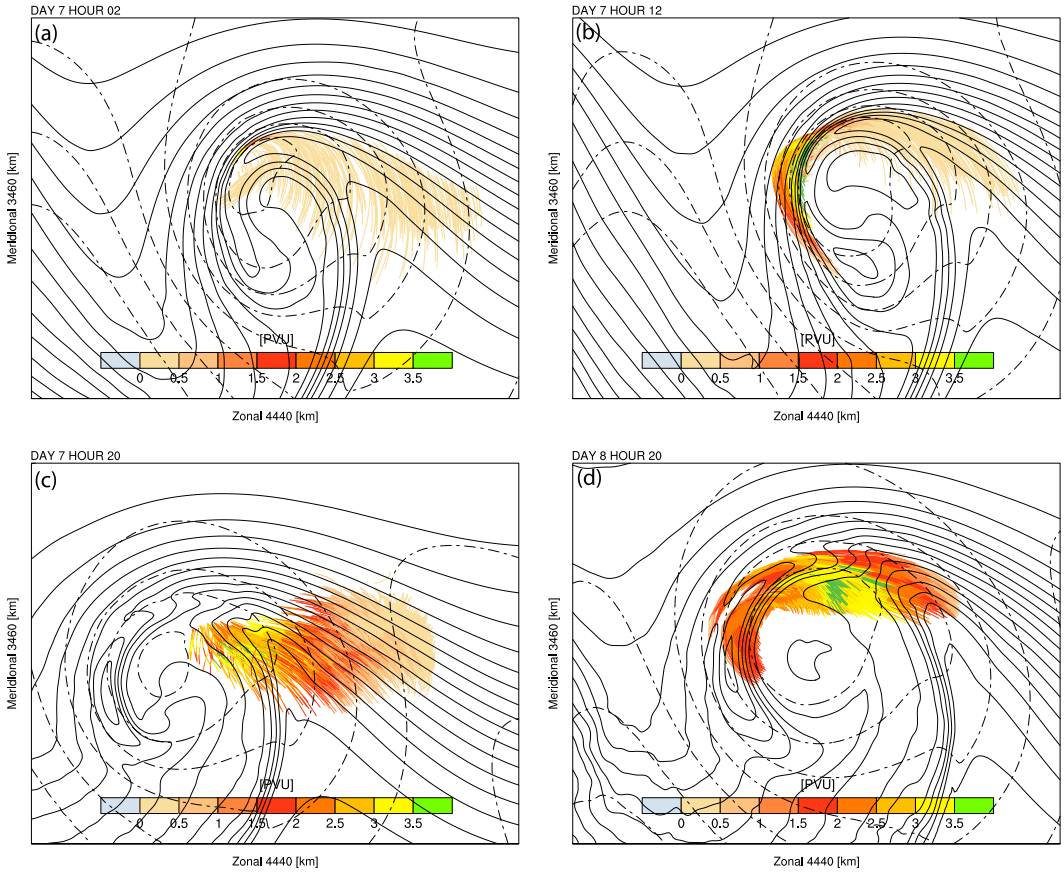

FIG. 4. CCB trajectories colored with PV for the (a),(b) idealized and (c),(d) extended simulations. Trajectories are shown during the last 10 h. Solid lines show contours of potential temperature at 850 hPa in steps of 2 K, and dashed contours show surface pressure (hPa) in steps of 10 hPa. In both cases, the number of CCB trajectories is around 1500.

cyclone and a reduction of PV to 0.2 PVU is occurring. The outflow is at 440 hPa, with potential temperature values of 315 K, corresponding to an increase of 20 K since the start at lower levels (not shown). The relevance of the strongly negative PV anomaly in the WCB outflow for the downstream development has been discussed in detail in Schemm et al. (2013).

In Figs. 3c and 3d, the WCB in the extended simulation is shown, which also starts in the warm sector and moves cyclonically toward higher latitudes in the narrowing warm sector. Diabatic PV modification becomes visible with high PV values of about 1.2 PVU (yellow coloring) at day 7, hour 8, especially for trajectories located at higher latitudes and along the cold front. The WCB trajectories reach upper levels in the cloud head at day 8, hour 10 (Fig. 3d), with reduced PV values below 0.3 PVU. The height of the WCB outflow in the extended simulation is 60 hPa above the outflow in the idealized simulation and at slightly higher values of θ (318 K compared to 315 K). The reason for the higher outflow and integrated latent heating in the extended simulation is the higher initial moisture content of the WCB, which is increased by ocean evaporation by roughly 2 g kg^{-1}.

c. *Principal airstream 2: The CCB*

The selected CCB trajectories are shown in Figs. 4a and 4b for the idealized run and in Figs. 4c and 4d for the extended simulation. Only the last 10 h are shown (i.e., not the entire 2-day period) in order to increase the visibility of the relevant features. The corresponding temporal evolution of pressure, potential temperature, specific humidity, and PV is shown in Fig. 5.

The CCB trajectories are initially located at higher latitudes compared to the WCB. In both simulations, the CCB starts at around 980 hPa (on average) and shows during the first day a smooth ascent by 20 hPa in the idealized case (light gray shading, Fig. 5a) and 5 hPa in the extended case (dark gray shading, Fig. 5a). In both runs, averaged values of θ remain fairly constant during the first day but differ significantly in their absolute values by 15 K (Fig. 5a). We find a similar difference for

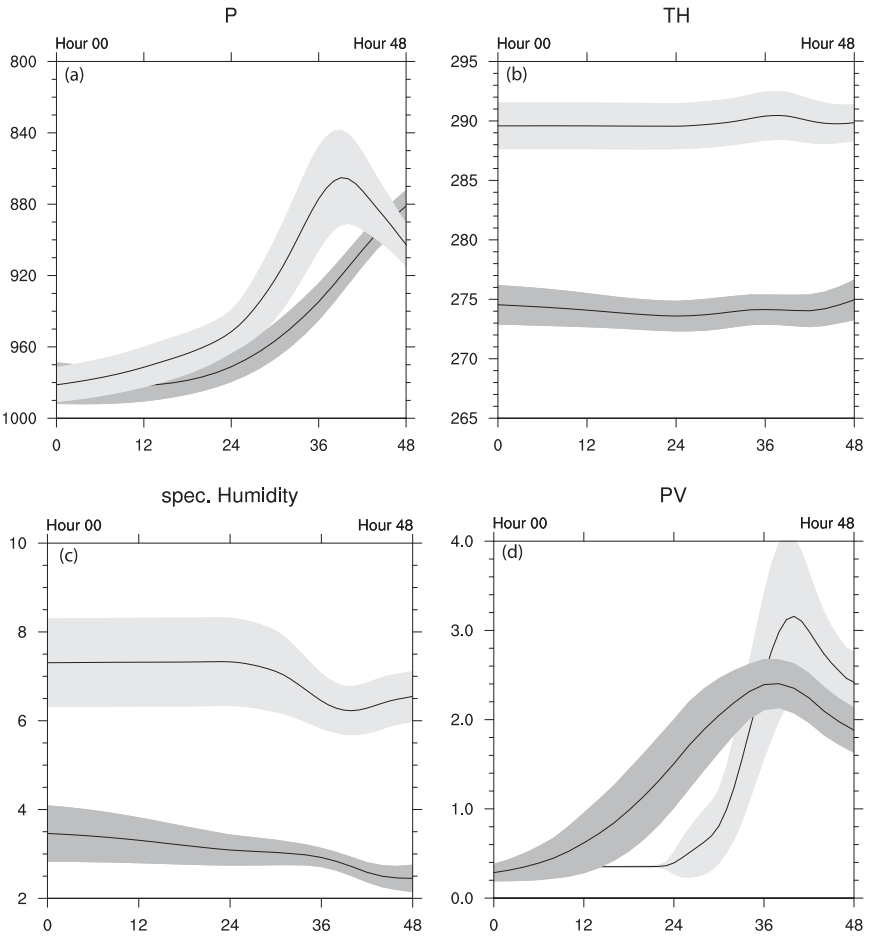

FIG. 5. Temporal evolution of several parameters along the CCB in the idealized (light gray) and extended simulations (dark gray). Black lines show averaged values for all CCB trajectories, and gray shading indicates the variability ($\pm 0.5\sigma$). Shown are (a) pressure (hPa), (b) potential temperature (K), (c) specific humidity ($g\,kg^{-1}$), and (d) PV (PVU). For both simulations, the number of trajectories is 1500.

specific humidity: the CCB in the idealized run is moister by almost $4\,g\,kg^{-1}$ (Fig. 5c). The decreased values of q_v and θ in the extended run stem from the different shape of the warm sector (Fig. 1). While the CCB starting positions in the idealized case are situated slightly to the east of the narrowing moist warm sector, the CCB starts in the extended run in a much drier and colder region where the warm sector is separated from the bent-back front (Figs. 4a,b).

The CCB moves against the direction of the eastward-propagating system along the bent-back front (Figs. 4b,d), which goes along with a moderate ascent to 870 hPa in the idealized case (Fig. 5a at hour 36) and 940 hPa in the extended case. During the first 24 h, q_v, θ, and PV are conserved in the idealized simulation (Figs. 5b–d), while the CCB in the extended case shows a weak decrease of q_v and θ (Figs. 5b,c; likely due to surface fluxes into the near-surface airstream). Potential vorticity increases to 3 PVU between hours 24 and 36 in the idealized run and starts to increase earlier with a peak value of 2.2 PVU around hour 36 in the extended simulation (Fig. 5d).

At the tail of the bent-back front, PV decreases for both CCBs (Figs. 4b,d and 5d). For the idealized case, the CCB descends during the last hours (Fig. 5a). Thus, cloud water droplets evaporate, which causes the observed increase in q_v, and in turn leads to the formation of a cooling maximum. The induced cooling maximum implies a decrease of PV below the level of maximum cooling. In the extended run, the CCB shows no descent during the final hours. However, a cooling maximum is present, which in this case is due to the evaporation of rain droplets from above and which is responsible for the slight decrease of PV values after hour 36.

In summary, we note that the selected CCB air parcels reach the tail of the bent-back front in both simulations with high PV. Qualitatively, the temporal PV evolution

TABLE 1. Change (%) of selected WCB and CCB trajectories with respect to the reference period (days 7–9) in the extended simulation.

Days	6–8	6.5–8.5	6.75–8.75
WCB	+70	+75	+40
CCB	−60	−33	−20

along the CCB in the extended simulation agrees well with the findings in the idealized simulation. The selected trajectories closely resemble the conceptual schematics of the cyclonic branch of the CCB by, for example, Schultz (2001) and Browning (2004). The CCB is confined to lower levels and moves along the colder side of the bent-back front cyclonically around the center of the low. Rossa et al. (2000) also identified low-level trajectories that show similarities to the identified CCB trajectories, in particular, a strong increase of PV, but without referring to the CCB concept.

We tested the sensitivity of the WCB and CCB criteria to the choice of the 48-h time period in the extended run. The number of identified trajectories for three shifted time periods is summarized in Table 1. It shows that WCB and CCB trajectories are also identified during other time periods. While the number of WCB trajectories increases for earlier periods, the number of CCB trajectories decreases. This points to an asymmetric evolution of strong vertical motion above the warm front and the horizontal motion along the growing bent-back front.

d. The effect of friction on the PV evolution along the WCB and CCB

The primary cause of diabatic changes of PV in both simulations is the release of latent heat. However, even in dry simulations, PV is generated in frontal regions because of numerical diffusion (Nakamura and Held 1989; Cooper et al. 1992; Bush and Peltier 1994; Stoelinga 1996). In this paragraph, we present an estimate of PV tendencies due to frictional processes along the calculated trajectories in the idealized run. To this end, we subtract from the overall PV change between two time steps the estimated PV tendency due to latent heating and consider the residual as the frictional PV tendency. The temperature tendency due to latent heating is a direct model output variable obtained from the saturation adjustment. In Fig. 6, the result is shown in the top row for the WCB and in the bottom row for the CCB.

The PV tendency due to the release of latent heat along the WCB (Fig. 6d) shows a fairly similar evolution compared to the total PV changes (Fig. 6a). Therefore, the frictional PV tendencies (Fig. 6c) remain weak and have no significant effect on the total PV tendency along the WCB.

For the CCB trajectories, total PV tendencies are larger than for the WCB (Fig. 6b). The results underpin the observed strong PV increase along the first intercept of the bent-back front induced by a strong midtropospheric heating rate maximum above the front. The frictional PV tendency is of lower amplitude compared to the PV tendencies due to latent heating (Fig. 6f), but in comparison with the WCB, the frictional PV tendency contributes more to the total tendency. During the strongest increase of PV, the frictional tendencies are also positive, and later they are negative and contribute to the decrease in PV. However, also in this simulation, the temporal evolution of the induced PV changes is dominated by the effect of latent heating (cf. Figs. 6d,e). More importantly, the integrated frictional PV tendency during the 2 days is close to zero, whereas the latent heating tendency is responsible for the net PV increase.

e. The CCB and the enhancement of the low-level jet

As shown previously, the CCB reaches the tail of the bent-back front with diabatically increased PV values. Here we briefly discuss the difference in the low-level wind field between the idealized run and a dry life cycle simulation. This dry run is described in detail by Schemm et al. (2013). No diabatic processes occur in the dry run, except for effects due to numerical diffusion, and the comparison therefore allows qualitatively estimating the diabatic influence on the low-level winds.

Figure 7 shows the low-level PV and wind vectors averaged between 1000 and 850 hPa for the idealized run and for the corresponding dry idealized run (initialized without moisture). The strongest differences (exceeding 2 PVU) are found along the northeastern region of the bent-back front, located below the midtropospheric heating maximum. In this region, we previously found the strongest gain of PV along the CCB trajectories. Subsequently, the high-PV air extends along the bent-back front toward its tail. The wind vectors reveal enhanced cyclonic winds in the idealized moist case compared to the dry simulation. However, note that the region of the strongest low-level wind in the moist run, shown by the green contour, is located at the tail of the bent-back front and is therefore in a different location compared to the maximum heating. Accordingly, the strongest gradient of PV is found in the region of maximum wind (not shown). The continuous advection of high, diabatically created PV air by the CCB along the bent-back front thus contributes to the observed enhancement of the strong low-level winds downstream of the diabatic PV production.

For the extended run, the CCB takes a similar path along the bent-back front; however, as described in section 3, the bent-back extension and the across-frontal

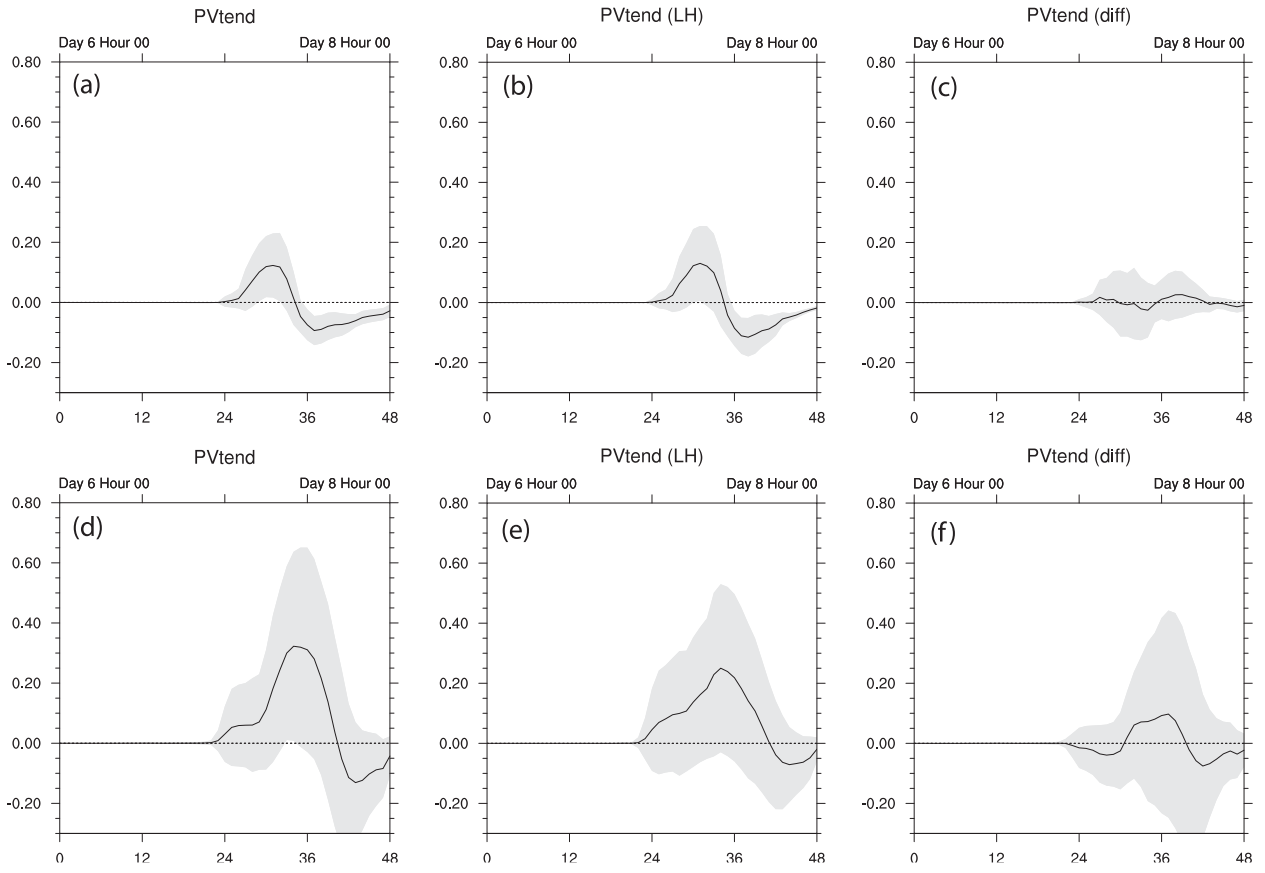

FIG. 6. Temporal evolution of PV tendencies along (a)–(c) WCB and (d)–(f) CCB. Shown are (left) total PV tendency, (center) PV tendency calculated due to latent heating, and (right) frictional tendencies.

pressure gradient are much weaker compared to the idealized case. The main reason for this is the downward flux of sensible heat that weakens the fronts, as shown below in Fig. 8. As a consequence, a weaker low-level jet at the tail of the bent-back front is found, but again with a strongly positive PV anomaly along the front (not shown). Although the low-level jet is weaker in the extended simulation, the findings are qualitatively similar to those presented above for the idealized run.

Strong and potentially damaging surface winds are frequently observed with the formation of a low-level jet along the bent-back front in an archetypal Shapiro–Keyser cyclone. Neiman et al. (1993) described the mesoscale evolution of a strongly intensifying cyclone during the Experiment on Rapidly Intensifying Cyclones over the Atlantic (ERICA) field campaign. They reported the formation of strong diabatic PV anomalies at lower levels along the warm front and the bent-back extension (and also found that frictional effects in the boundary layer are of minor importance) and highest wind speeds along the colder side of the warm-air seclusion. Grønås (1995) discussed in great detail the seclusion process of warm air by the bent-back front and the often observed reintensification of the system during the seclusion. He described the formation of a strong low-level jet on the basis of a numerical simulation of the New Year's Day storm of 1992 and emphasized the particular role of latent heat release and diabatic PV modification along the bent-back front during the seclusion of warm air masses by colder air. In his analysis of the damaging surface winds and mesoscale structures of the Great Storm of 1987 over southeastern England, Browning (2004) found a strong low-level jet along the tail of the bent-back front and associated its formation with not only the CCB, but also with the sting jet. Similar observations are made in the study of Hulme and Martin (2009) during the extratropical transition of Hurricane Karen, however, with a focus on the generation of vorticity by stretching and subsequent advection along the bent-back front without explicitly making a reference to the CCB. In a recent case study of an intense extratropical cyclone over northern Ireland in January 2012, Smart and Browning

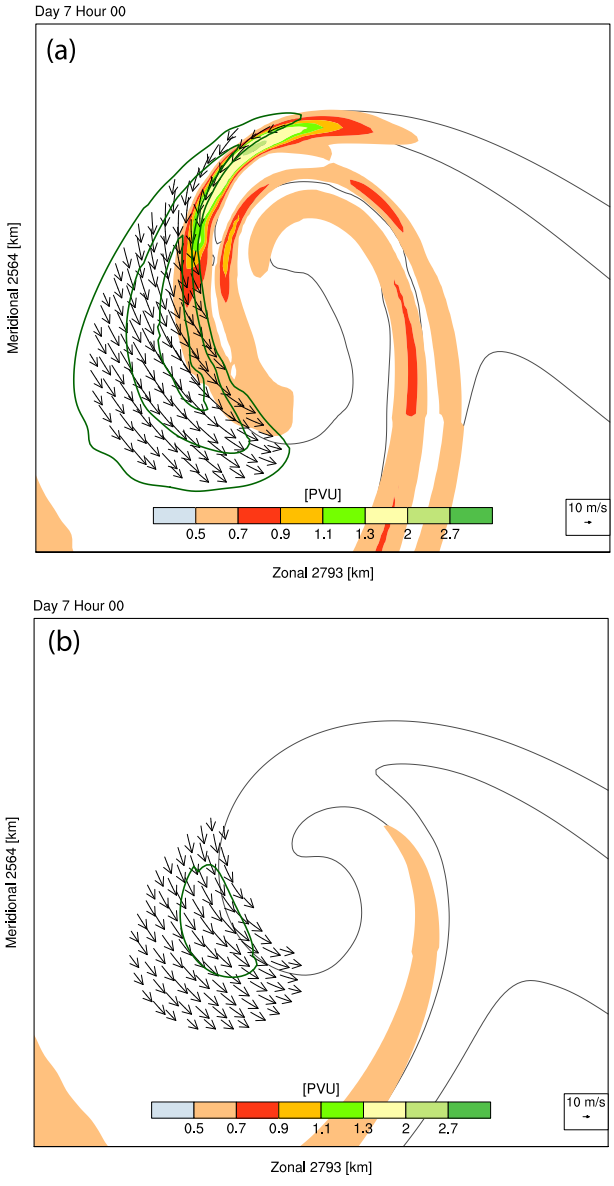

FIG. 7. Low-level vertically averaged (1000–850 hPa) PV and wind for (a) the moist idealized simulation and (b) a dry simulation. Also shown are the 290-, 295-, and 300-K isentropes at 850 hPa and the region of strong low-level wind (30, 35, and 40 m s^{-1}; green contours).

(2014) emphasized the role of the CCB for the formation of strong wind gusts along the bent-back front. They attributed most of the strong surface wind gusts to the CCB and only very short peak gusts to the sting jet. The importance of the low-level PV anomaly for the intensification of the cyclone has been shown in a case study by Stoelinga (1996), by means of a PV inversion. These examples from simulated real storms suggest the significance of the intense winds associated with the diabatic PV increase along the CCB.

5. The linkage between the WCB and the CCB

Detailed analysis of the two airstreams revealed that the observed increase of PV along the CCB and WCB trajectories are associated with the same midtropospheric maximum of latent heat release above the bent-back front. This becomes evident from two vertical north–south cross sections shown in Fig. 8a for the idealized run and in Fig. 8b for the extended run. In the upper-left corner of the panels, the precise location of the cross sections is shown. A pronounced positive PV tendency (red color) is found below the level of maximum heating rate (solid black contours) and a negative signal is found above the maximum (blue colors). In the idealized case, latent heating of 0.25 K h^{-1} occurs up to 400 hPa, while in the extended run, it extends further up, to approximately 350 hPa. Maximum values of latent heat release and PV tendencies are significantly enhanced in the extended case compared to the idealized run.

We calculated the intersections of the WCB (red asterisks) and the CCB trajectories (blue asterisks) with both vertical planes. In Fig. 8a, the rising WCB air is forming the region of maximum latent heating between 700 and 800 hPa. At the same time, the CCB located below this region is situated at the colder side of the front and thereby gains PV. In Fig. 8b, we find a comparable result, with the majority of WCB air parcels situated at approximately 600 hPa in the center of maximum heating and the CCB moving below this region. As the bent-back front is less strong in the extended run, the CCB moves on almost horizontal isentropes. Negative PV tendencies on both sides of the front are associated with evaporating precipitation or cloud droplets.

From these two cross sections, it becomes evident that the gain of PV along the CCB is directly related to the strength of the latent heat release induced by the WCB. PV along the CCB, especially the increase of PV along the bent-back front, is therefore inherently linked to the vertically rising moist air masses of the WCB. Similar observational-based cross sections of Neiman et al. (1993, Fig. 12) revealed comparable results but did not include WCB and CCB intersection points.

6. Summary and conclusions

We presented a method to identify the cyclonic branch of the CCB and the WCB as coherent bundles of trajectories. A pressure–PV scatterplot was used to summarize the relationship between the formation of PV anomalies and vertical ascent of low-level air parcels in a growing cyclone (Fig. 2). The WCB and the CCB could be identified from this pressure–PV scatterplot as two coherent air masses that are associated with the

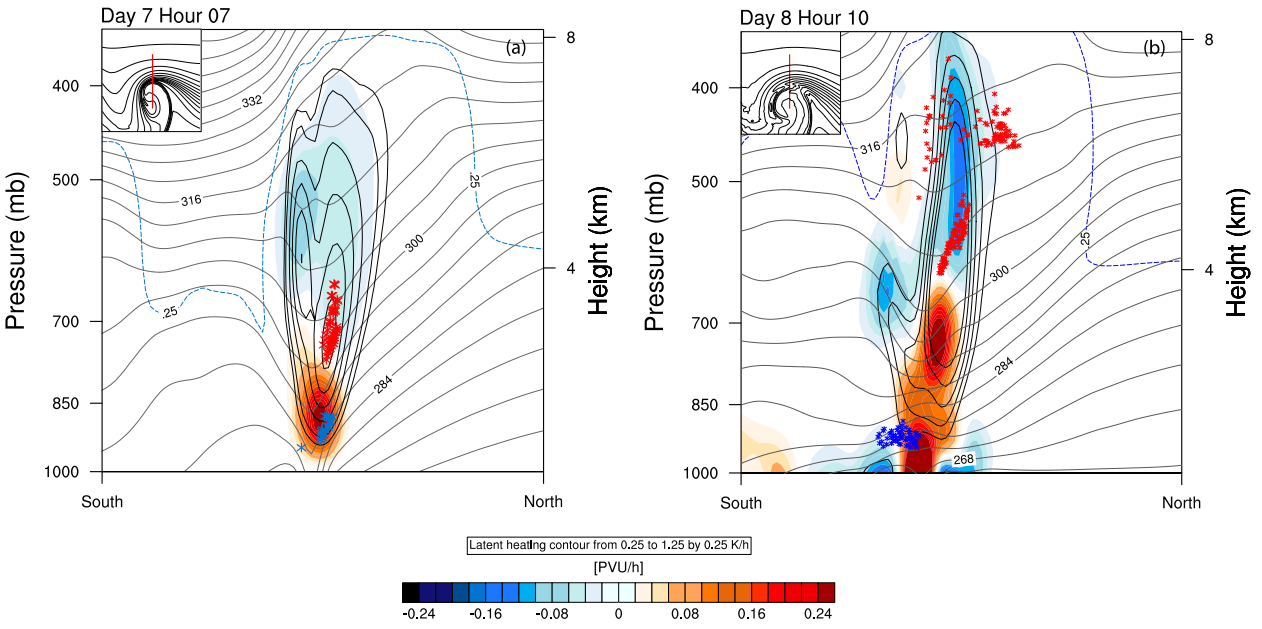

FIG. 8. Vertical cross sections through the bent-back front for the (a) idealized and (b) extended simulations. The exact position of the cross sections is shown in the insets. Shown are contours of condensational heating (thick black lines; every 0.25 K h^{-1}); colors show diabatic PV tendencies (PVU h^{-1}), thin gray contours show potential temperature (K), and the dashed blue contours indicate 0.25 g kg^{-1} of specific humidity. Intersection of the WCB trajectories with the cross section is shown by red asterisks and of the CCB trajectories with the cross section is shown by blue asterisks.

formation of a strong positive PV anomaly at lower-tropospheric levels along the bent-back front (CCB) and a strong negative PV anomaly at upper-tropospheric levels (WCB).

Therefore, inferred from the pressure–PV scatterplot, we can relate the PV characteristics of the WCB and CCB to two important dynamical impacts, which are the enhancement of downstream cyclogenesis due to the perturbation of the Rossby waveguide (WCB) and the enhancement of the low-level jet along the tail of the bent-back front (CCB). The previously mentioned conclusion on the downstream modification is discussed primarily in our first idealized study (Schemm et al. 2013) and mentioned here for completeness.

In more detail, we use Lagrangian criteria to identify

- the WCB as the air parcels with a maximum ascent given a suitable period of time, typically 48 h (as in previous studies), and
- the cyclonic branch of the CCB by a starting position at low levels, a final position 48 h later also at low levels, and an increase of PV above a suitable threshold at least once during the 48 h.

The precise values of ascent in a given time period (WCB) or the PV threshold (CCB) can vary from case to case, and in particular, the applicability of the definition of the CCB needs to be tested further in real case studies.

To summarize the linkage between the WCB and the CCB, consider the schematic in Fig. 9, which shows contours of surface isentropes (solid) and isobars (dashed) and, at upper levels, the meandering motion of the jet stream (orange contour). The strongest vertical motion in the warm sector of the cyclone manifests itself in the formation of the WCB, shown in green, which is ascending above the bent-back front. At upper-tropospheric levels, this WCB slopes into the direction of the prevailing, typically zonal, winds. At midtropospheric levels, a prominent maximum of heating rate is shown, indicated by the reddish colors. The thusly induced diabatic PV changes in the vicinity of the heating rate maximum are denoted by the red plus and minus signs, and both resulting PV anomalies are encircled by their associated cyclonic or anticyclonic circulation, respectively. As discussed with a similar idealized setup by Schemm et al. (2013), the WCB outflow forms a negative PV anomaly at upper levels, which perturbs the Rossby waveguide, and the anticyclonic vorticity around the WCB outflow leads to an enhancement of the downstream cyclogenesis.

The cyclonic branch of the CCB is shown in blue in Fig. 9. It originates, in contrast to the WCB, at higher latitudes and moves, in the case of an eastward-traveling system, rearward along the colder side of the bent-back front. The CCB gains PV below the heating maximum,

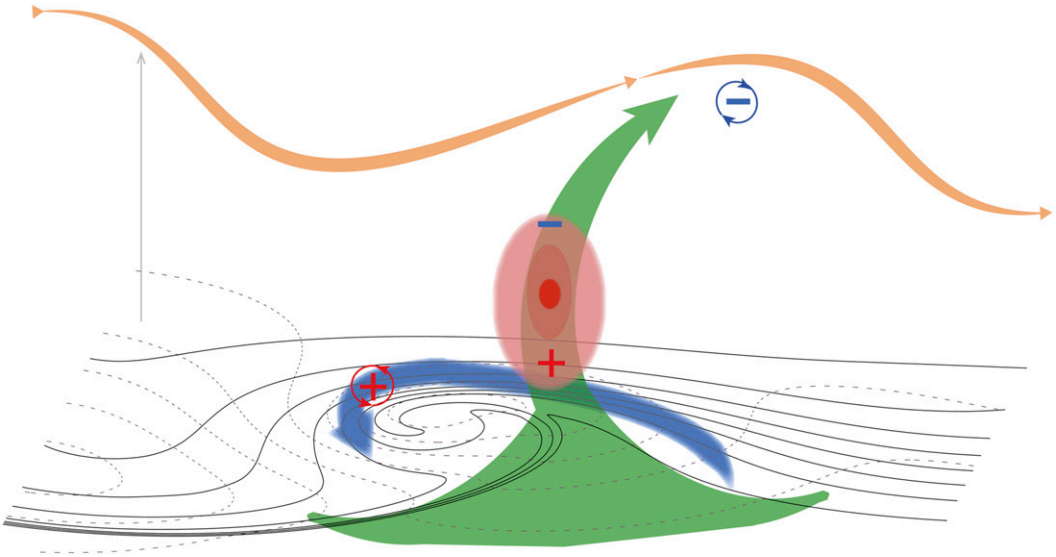

FIG. 9. A conceptual model of the interaction between the WCB (green arrow) and the CCB (blue arrow), the induced diabatic PV tendencies (plus and minus signs), and the resulting circulation anomalies at the end of the airstreams. A maximum region of diabatic heating (reddish colors) is formed at midtropospheric levels due to the ascending WCB. Also shown is the upper-level jet stream (orange line), where the WCB induces a stronger anticyclonic curvature of the flow and, because of the increase of the PV gradient, higher wind speeds. At lower levels, the CCB induces a stronger cyclonic curvature and enhances the wind speeds along the tail of the bent-back front.

which is formed by the ascending WCB and, as a consequence, advects high-PV air toward the tail of the bent-back front. This finding is qualitatively similar to the formation of relative vorticity maxima along the bent-back front in Takayabu (1986) and Wernli et al. (1998), but it emphasizes the effect of latent heating on PV. The steady and rapid increase of vorticity and PV along the air parcels moving along the bent-back extension of the warm front points to the intrinsic three-dimensional nature of the structure of the warm front (Schär and Wernli 1993).

This linkage between the WCB and CCB is a key result of this study, as it highlights, in the framework of a prototype baroclinic wave development, how the latent heating in the WCB both leads to the formation of an intense low-level jet along the bent-back front and its tail and to an accelerated downstream development at the tropopause level.

The findings from our idealized simulation, which comprises solely the effects of condensation and evaporation, are robust if compared to an enhanced simulation, which incorporates surface fluxes, moist convection, and small-scale boundary layer turbulence. Hence, the findings summarized above can be considered as archetypal for the simulated type of extratropical cyclones. An interesting difference occurs along the bent-back front where the cross-frontal gradients of pressure and temperature are reduced in the extended compared to the idealized case. In real case studies of cyclones, ice-phase processes in the upper troposphere (predominantly from depositional growth of snow; Joos and Wernli 2012) can additionally alter the PV along the WCB. These processes are not taken into account in our extended simulation.

In a next step, our findings on the linkage between the WCB and CCB need to be confirmed by real case studies. It would be interesting in such studies to reproduce the pressure–PV scatterplot.

A video visualization of the WCB and CCB in the idealized run presented in this study can be found in the supplemental material, which further helps to support the schematic summary shown in Fig. 9.

Acknowledgments. Sebastian Schemm acknowledges funding from the Swiss National Science Foundation (Project 200021-130079). We thank David Schultz and two anonymous reviewers for their helpful comments. All figures, except Fig. 2, have been produced with the NCAR Command Language.

REFERENCES

Agustí-Panareda, A., S. L. Gray, and S. E. Belcher, 2009: On the dependence of boundary-layer ventilation on frontal type. *J. Geophys. Res.,* **114,** D05305, doi:10.1029/2008JD010694.

Bader, M. J., G. S. Forbes, J. R. Grant, R. B. E. Lilley, and A. J. Waters, 1995: *Images in Weather Forecasting.* Cambridge University Press, 499 pp.

Bigelow, F., 1902: Circulation of the atmosphere in high and low areas. *Mon. Wea. Rev.,* **30,** 117–125.

Boutle, I. A., S. E. Belcher, and R. S. Plant, 2011: Moisture transport in midlatitude cyclones. *Quart. J. Roy. Meteor. Soc.,* **137,** 360–373.

Brennan, M. J., G. M. Lackmann, and K. M. Mahoney, 2008: Potential vorticity PV thinking in operations: The utility of nonconservation. *Wea. Forecasting,* **23,** 168–182.

Browning, K. A., 1986: Conceptual models of precipitation systems. *Wea. Forecasting,* **1,** 23–41.

——, 1990: Organisation of clouds and precipitation in extratropical cyclones. *Extratropical Cyclones: The Erik Palmén Memorial Volume,* C. W. Newton and E. O. Holopainen, Eds., Amer. Meteor. Soc., 129–165.

——, 2004: The sting at the end of the tail: Damaging winds associated with extratropical cyclones. *Quart. J. Roy. Meteor. Soc.,* **130,** 375–399.

——, and N. M. Roberts, 1994: Structure of a frontal cyclone. *Quart. J. Roy. Meteor. Soc.,* **120,** 1535–1557.

Bush, A. B. G., and W. R. Peltier, 1994: Tropopause folds and synoptic-scale baroclinic wave life cycles. *J. Atmos. Sci.,* **51,** 1581–1604.

Čampa, J., and H. Wernli, 2012: A PV perspective on the vertical structure of mature midlatitude cyclones in the Northern Hemisphere. *J. Atmos. Sci.,* **69,** 725–740.

Carlson, T. N., 1980: Airflow through midlatitude cyclones and the comma cloud pattern. *Mon. Wea. Rev.,* **108,** 1498–1509.

Clark, P. A., K. A. Browning, and C. Wang, 2005: The sting at the end of the tail: Model diagnostics of fine-scale three-dimensional structure of the cloud head. *Quart. J. Roy. Meteor. Soc.,* **131,** 2263–2292.

Cooper, I. M., A. J. Thorpe, and C. G. Bishop, 1992: The role of diffusive effects on potential vorticity in fronts. *Quart. J. Roy. Meteor. Soc.,* **118,** 629–647.

Crocker, A. M., W. L. Godson, and C. M. Penner, 1947: Frontal contour charts. *J. Meteor.,* **4,** 95–99.

Davis, C. A., and K. A. Emanuel, 1991: A potential vorticity diagnostics of cyclogenesis. *Mon. Wea. Rev.,* **119,** 1929–1953.

Eckhardt, S., A. Stohl, H. Wernli, P. James, C. Forster, and N. Spichtinger, 2004: A 15-year climatology of warm conveyor belts. *J. Climate,* **17,** 218–237.

Eliassen, A., and E. Kleinschmidt, 1957: Dynamic meteorology. *Handbuch der Physik,* S. Flügge, Ed., Springer-Verlag, 1–154.

Galloway, J. L., 1958: The three-front model: Its philosophy, nature, construction and use. *Weather,* **13,** 3–10.

Godson, W. L., 1951: Synoptic properties of frontal surfaces. *Quart. J. Roy. Meteor. Soc.,* **77,** 633–653.

Grams, C. M., and Coauthors, 2011: The key role of diabatic processes in modifying the upper-tropospheric wave guide: A North Atlantic case-study. *Quart. J. Roy. Meteor. Soc.,* **137,** 2174–2193.

Green, J. S. A., F. H. Ludlam, and J. F. R. McIlven, 1966: Isentropic relative-flow analysis and the parcel theory. *Quart. J. Roy. Meteor. Soc.,* **92,** 210–219.

Grønås, S., 1995: The seclusion intensification of the New Year's Day storm 1992. *Tellus,* **47A,** 733–746.

Harrold, T. W., 1973: Mechanisms influencing distribution of precipitation within baroclinic disturbances. *Quart. J. Roy. Meteor. Soc.,* **99,** 232–251.

Haynes, P. H., and M. E. McIntyre, 1987: On the evolution of vorticity and potential vorticity in the presence of diabatic heating and frictional or other forces. *J. Atmos. Sci.,* **44,** 828–841.

Herzog, H.-J., G. Vogel, and U. Schubert, 2002: LLM—A nonhydrostatic model applied to high-resolving simulations of turbulent fluxes over heterogeneous terrain. *Theor. Appl. Climatol.,* **73,** 67–86.

Hines, K. M., and C. R. Mechoso, 1993: Influence of surface drag on the evolution of fronts. *Mon. Wea. Rev.,* **121,** 1152–1176.

Hoskins, B. J., M. E. McIntyre, and A. W. Robertson, 1985: On the use and significance of isentropic potential vorticity maps. *Quart. J. Roy. Meteor. Soc.,* **111,** 877–946.

Hulme, A. L., and J. E. Martin, 2009: Synoptic- and frontal-scale influences on tropical transition events in the Atlantic basin. Part II: Tropical transition of Hurricane Karen. *Mon. Wea. Rev.,* **137,** 3626–3650.

Joos, H., and H. Wernli, 2012: Influence of microphysical processes on the potential vorticity development in a warm conveyor belt: A case study with the limited-area model COSMO. *Quart. J. Roy. Meteor. Soc.,* **138,** 407–418.

Kessler, E., 1969: *On the Distribution and Continuity of Water Substance in the Atmospheric Circulations. Meteor. Monogr.,* No. 32, Amer. Meteor. Soc., 84 pp.

Keyser, D., and R. Rotunno, 1990: On the formation of potential-vorticity anomalies in upper-level jet-front systems. *Mon. Wea. Rev.,* **118,** 1914–1921.

Kuo, Y.-H., R. J. Reed, and S. Low-Nam, 1992: Thermal structure and airflow in a model simulation of an occluded marine cyclone. *Mon. Wea. Rev.,* **120,** 2280–2297.

Madonna, E., H. Wernli, H. Joos, and O. Martius, 2014: Warm conveyor belts in the ERA-Interim data set (1979–2010). Part I: Climatology and potential vorticity evolution. *J. Climate,* **27,** 3–26, doi:10.1175/JCLI-D-12-00720.1.

Martin, J. E., 1999: Quasigeostrophic forcing of ascent in the occluded sector of cyclones and the trowal airstream. *Mon. Wea. Rev.,* **127,** 70–88.

Martínez-Alvarado, O., F. Weidle, and S. L. Gray, 2010: Sting jets in simulations of a real cyclone by two mesoscale models. *Mon. Wea. Rev.,* **138,** 4054–4075.

Mass, C. F., and D. M. Schultz, 1993: The structure and evolution of a simulated midlatitude cyclone over land. *Mon. Wea. Rev.,* **121,** 889–917.

Mellor, G., and T. Yamada, 1982: Development of a turbulence closure model for geophysical fluid problems. *Rev. Geophys. Space Phys.,* **20,** 851–875.

Nakamura, N., and I. M. Held, 1989: Nonlinear equilibrium of two-dimensional Eady waves. *J. Atmos. Sci.,* **46,** 3055–3064.

Namias, J., 1939: The use of isentropic analysis in short term forecasting. *J. Aeronaut. Sci.*, **6**, 295–298.

Neiman, P. J., M. A. Shapiro, and L. S. Fedor, 1993: The life cycle of an extratropical marine cyclone. Part II: Mesoscale structure and diagnostics. *Mon. Wea. Rev.,* **121,** 2177–2199.

Penner, C. M., 1955: A three-front model for synoptic analyses. *Quart. J. Roy. Meteor. Soc.,* **81,** 89–91.

Pomroy, H. R., and A. J. Thorpe, 2000: The evolution and dynamical role of reduced upper-tropospheric potential vorticity in Intensive Observing Period One of FASTEX. *Mon. Wea. Rev.,* **128,** 1817–1834.

Raymond, D. J., and H. Jiang, 1990: A theory for long-lived mesoscale convective systems. *J. Atmos. Sci.,* **47,** 3067–3077.

Reed, R. J., M. T. Stoelinga, and Y.-H. Kuo, 1992: A model-aided study of the origin and evolution of the anomalously high potential vorticity in the inner region of a rapidly deepening marine cyclone. *Mon. Wea. Rev.,* **120,** 893–913.

——, Y.-H. Kuo, and S. Low-Nam, 1994: An adiabatic simulation of the ERICA IOP 4 storm: An example of quasi-ideal frontal cyclone development. *Mon. Wea. Rev.,* **122,** 2688–2708.

Rossa, A. M., H. Wernli, and H. C. Davies, 2000: Growth and decay of an extra-tropical cyclone's PV-tower. *Meteor. Atmos. Phys.,* **73,** 139–156.

Rotunno, R., W. C. Skamarock, and C. Snyder, 1998: Effects of surface drag on fronts within numerically simulated baroclinic waves. *J. Atmos. Sci.,* **55,** 2119–2129.

Schär, C., and H. Wernli, 1993: Structure and evolution of an isolated semi-geostrophic cyclone. *Quart. J. Roy. Meteor. Soc.,* **119,** 57–90.

Schemm, S., H. Wernli, and L. Papritz, 2013: Warm conveyor belts in idealized moist baroclinic wave simulations. *J. Atmos. Sci.,* **70,** 627–652.

Schultz, D. M., 2001: Reexamining the cold conveyor belt. *Mon. Wea. Rev.,* **129,** 2205–2225.

——, and C. F. Mass, 1993: The occlusion process in a midlatitude cyclone over land. *Mon. Wea. Rev.,* **121,** 918–940.

Shapiro, M. A., 1976: The role of turbulent heat flux in the generation of potential vorticity in the vicinity of upper-level jet stream systems. *Mon. Wea. Rev.,* **104,** 892–906.

——, 1978: Further evidence of the mesoscale and turbulent structure of upper-level jet stream-frontal systems. *Mon. Wea. Rev.,* **106,** 1100–1111.

——, and D. Keyser, 1990: Front, jet streams and the tropopause. *Extratropical Cyclones: The Erik Palmén Memorial Volume,* C. W. Newton and E. O. Holopainen, Eds., Amer. Meteor. Soc., 167–191.

Shaw, W. N., and R. G. K. Lempfert, 1906: *The Life History of Surface Air Currents: A Study of the Surface Trajectories of Moving Air Masses.* Darling and Son, Ltd., 107 pp.

Sinclair, V. A., S. L. Gray, and S. E. Belcher, 2008: Boundary-layer ventilation by baroclinic life cycles. *Quart. J. Roy. Meteor. Soc.,* **134,** 1409–1424.

Smart, D. J., and K. A. Browning, 2014: Attribution of strong winds to a cold conveyor belt and sting jet. *Quart. J. Roy. Meteor. Soc.,* doi:10.1002/qj.2162, in press.

Stoelinga, M. T., 1996: A potential vorticity-based study of the role of diabatic heating and friction in a numerically simulated baroclinic cyclone. *Mon. Wea. Rev.,* **124,** 849–874.

Stohl, A., 2001: A 1-year Lagrangian climatology of airstreams in the Northern Hemisphere troposphere and lowermost stratosphere. *J. Geophys. Res.,* **106,** 7263–7279, doi:10.1029/2000JD900570.

Takayabu, I., 1986: Roles of the horizontal advection on the formation of surface fronts and on the occlusion of a cyclone developing in the baroclinic westerly jet. *J. Meteor. Soc. Japan,* **64,** 329–345.

Thompson, W. T., 1995: Numerical simulations of the life cycle of a baroclinic wave. *Tellus,* **47A,** 722–732.

Tiedtke, M., 1989: A comprehensive mass flux scheme for cumulus parameterization in large-scale models. *Mon. Wea. Rev.,* **117,** 1779–1799.

Wernli, H., 1997: A Lagrangian-based analysis of extratropical cyclones II. A detailed case study. *Quart. J. Roy. Meteor. Soc.,* **123,** 1677–1706.

——, and H. C. Davies, 1997: A Lagrangian-based analysis of extratropical cyclones I. The method and some applications. *Quart. J. Roy. Meteor. Soc.,* **123,** 467–489.

——, R. Fehlmann, and D. Lüthi, 1998: The effect of barotropic shear on upper-level induced cyclogenesis: Semigeostrophic and primitive equation numerical simulations. *J. Atmos. Sci.,* **55,** 2080–2094.

——, S. Dirren, M. A. Liniger, and M. Zillig, 2002: Dynamical aspects of the life cycle of the winter storm ''Lothar.'' *Quart. J. Roy. Meteor. Soc.,* **128,** 405–429.

Whitaker, J. S., L. W. Uccellini, and K. F. Brill, 1988: A model-based diagnostic study of the rapid development phase of the Presidents's Day cyclone. *Mon. Wea. Rev.,* **116,** 2337–2365.

Young, M. V., G. A. Monk, and K. A. Browning, 1987: Interpretation of satellite imagery of a rapidly deepening cyclone. *Quart. J. Roy. Meteor. Soc.,* **113,** 1089–1115.